DISCLAIMER

LA-UR-25-31376

Approved for public release; distribution is unlimited.

Title:	Using molecular dynamics simulations to validate a new approach for determining the melting curves of materials
Author(s):	Farnault, Bastien Henri
Intended for:	Report
Issued:	2025-11-18

National Graduate School of Materials, Food Engineering, and Chemistry

2nd Year of Engineering Program

Specialization in Chemistry and Physical Engineering

Internship Report

Bastien Henri Farnault

June 2nd – November 14th, 2025

Los Alamos National Laboratory, P.O. Box 1663, Los Alamos, NM 87545

Using molecular dynamics simulations to validate a new approach for determining the melting curves of materials

Mentor : Dr. Jérôme Daligault

Co-Mentor: Dr. Alfred Farris

Academic Advisor: Sandra Pinet

Acknowledgments

I would like to express my sincere gratitude to all those who contributed to the success of this internship.

First and foremost, I would like to warmly and sincerely thank **Dr. Jérôme Daligault**, my professional supervisor and physicist at Los Alamos National Laboratory, for his kindness, high standards, guidance, numerous pieces of advice, and continuous support throughout this 24-week internship. I am also deeply grateful for his trust and for the opportunity to work alongside him each day, which made this experience both inspiring and truly enjoyable.

I would also like to thank **Dr. Alfred Farris**, whose expertise and mentorship greatly enriched my research experience and helped me develop new scientific perspectives.

My warm thanks go to **Dr. Romain Perriot**, physicist at Los Alamos, for his help in securing this internship and for his valuable advice during our many discussions throughout the course of this work.

I also wish to express my sincere appreciation to **Dr. Cédric Crespos**, Program Director of the international Master's degree in Physical Chemistry and Chemical Physics (PCCP), researcher in Theoretical Chemistry at the ISM (UMR CNRS 5255), and lecturer at the University of Bordeaux and ENSMAC. His support during the search for this internship was invaluable; without his assistance, this opportunity would not have been possible.

I would also like to express my warmest gratitude to **Dr. Abigail Hunter** (Group Leader, XCP-5) for her invaluable assistance with the laboratory's administrative procedures, as well as for approving my visit to Los Alamos National Laboratory. I am equally grateful for her support in extending our collaboration with the division upon my return to France.

My thanks also go to **Leah Hartman** and **Naomi Raicu**, Ph.D. students at the University of Michigan (MI), with whom I had the pleasure of collaborating for several months. I am very grateful for their help, insightful advice, and the stimulating discussions we shared. It was a great pleasure to work and exchange ideas with two American students and to contribute together to a shared scientific vision.

My gratitude extends to **Sandra Pinet**, my academic advisor at ENSMAC, for her continuous support, valuable feedback, and encouragement throughout this project.

I would also like to express my sincere appreciation to several members of the **ENSMAC administration**: **Laurence Vignau** (Program Director), **Bénédicte Paule** (Head of International Relations), and **Pascale-Emmanuelle Fayet Masson** (Department Administrator for CGP), for their valuable assistance and availability during the preparation of my administrative file required by Los Alamos National Laboratory.

Finally, I wish to thank my colleagues, friends, my parents, my sister, and my family for their constant encouragement and support throughout this professional and personal journey.

This page is intentionally left blank.

Contents

1 Introduction: The Los Alamos National Laboratory

The Los Alamos National Laboratory (LANL), located in the state of New Mexico (United States), is one of the most iconic research centers in the world. Founded in 1943 as part of the Manhattan Project [1, 2], it emerged from a global conflict and an unprecedented scientific emergency. At that time, the United States feared that Nazi Germany might develop an atomic weapon first. Under the direction of physicist J. Robert Oppenheimer [3], the U.S. government established a secret laboratory in an isolated region of the Los Alamos plateau, bringing together some of the greatest scientific minds of the era. This site, then known as *Project Y*, became the birthplace of the first atomic bomb.

During World War II, Los Alamos became an extraordinary center of intellectual collaboration. Physicists, chemists, engineers, and mathematicians from around the world — including Enrico Fermi, Richard Feynman, and Niels Bohr — joined forces to accomplish a mission considered crucial for ending the war [4]. It was here that the "Little Boy" and "Fat Man" bombs were designed, later dropped on Hiroshima and Nagasaki in August 1945. On July 16, 1945, the laboratory carried out the first nuclear test in history, known as the *Trinity* test [5], conducted in the New Mexico desert. This event marked the beginning of the atomic age and profoundly transformed the relationship between science, technology, and political power.

After the war, Los Alamos continued its work within the context of the Cold War, becoming a central player in nuclear weapons research and U.S. strategic deterrence [6]. New facilities were built to develop more advanced weapons as well as technologies for detection, safety, and simulation. From the 1960s onward, the laboratory broadened its mission toward civil and scientific fields such as energy, astrophysics, materials chemistry, biotechnology, and high-performance computing [7]. This diversification marked a turning point: LANL evolved from a military-oriented institution into a multidisciplinary research center serving both science and society.

Today, Los Alamos National Laboratory employs over 14,000 people and operates with an annual budget of several billion dollars [8]. It remains under the supervision of the Department of Energy (DOE) and plays a key role not only in national security and nuclear non-proliferation, but also in leading scientific programs in advanced simulation, artificial intelligence, climate research, nuclear fusion, materials science, and renewable energy. Among its most renowned facilities are the *Trinity* supercomputer — one of the most powerful in the world [9] — and several research laboratories open to international collaboration.

LANL's mission is to "solve national security challenges through simultaneous excellence." The laboratory strives to achieve significant impact on strategic priorities by combining world-class research and development with operational excellence and strong community engagement [10]. As a federally funded research and development center, LANL aligns its strategic plan with the priorities set by the DOE's National Nuclear Security Administration (NNSA) and other national strategy frameworks. It conducts work across all DOE missions: national security, science, energy, and environmental management. The scientific and engineering expertise developed over decades of research remains at the core of what makes LANL, DOE, and NNSA a major driving force of science, technology, and innovation in the United States.

2 Context and Objectives

2.1 Project inception

Determining the melting curve of a material is a key thermodynamic objective with far-reaching implications across materials physics, high-pressure engineering, and planetary sciences [11] . Melting curves are essential for assessing the stability of structural and nuclear materials under extreme conditions, and they also provide valuable constraints on planetary interiors, evolutionary models, and various astrophysical observations. Beyond these practical aspects, they can reveal profound changes in atomic bonding under compression, several of which have recently been highlighted by high-pressure experiments.[12] [13].

Despite their importance, melting curves remain difficult to determine with precision, especially at high pressures and temperatures. Molecular simulations offer an important complementary route, but most standard approaches free-energy calculations, two-phase coexistence, or the Z-method require prior identification of the stable solid phase. This step becomes challenging whenever compression induces competing crystalline structures, as is the case for alkali metals, which exhibit a sequence of complex and sometimes poorly understood structural transitions, along with non-monotonic melting behavior and unusual electronic features.

These limitations naturally raise the question of whether the melting transition can be predicted directly from liquid-state dynamics, without any knowledge of the solid phase. Several empirical freezing criteria have been proposed, particularly for hard-sphere and Lennard–Jones systems. Among them, the Hansen–Verlet rule is often cited: crystallization is expected when the height of the first peak of the static structure factor $S(k)$ reaches approximately 2.85[14] . While useful in simple cases, this threshold is not universal and loses reliability for systems with more complex interactions, such as compressed alkali metals.[15, 16]

In this work, we adopt a different perspective by analyzing liquid-state dynamics through the statistics of atomic displacements, using *first-passage times* (FPT). This quantity measures the average time required for an atom to travel a given distance for the first time. It provides direct insight into the onset of dynamical hindrance in the liquid and reveals a clear signature of the approach to freezing. This leads to a simple and transferable criterion for locating the melting point along an isochor or isobar, without simulating the solid phase.

To formalize this idea, we introduce the mean first-passage time:

$$T(r) = \int_0^\infty F_r(t)\, t\, dt,$$

which represents the average time needed for an atom to move a distance r from its initial position. This quantity is readily obtained from molecular dynamics trajectories by analyzing the distribution of first-passage events.

Instead of examining $T(r)$ directly, we consider its logarithmic derivative:

$$D(r) = \frac{d \ln T(r)}{d \ln r},$$

which describes how the characteristic timescale of atomic motion grows with displacement. Being dimensionless, $D(r)$ allows straightforward comparison across interaction models and thermodynamic conditions. Most importantly, it exhibits robust and reproducible features: as shown in Fig. X, $D(r)$ displays a well-defined peak near $r^* \approx 0.7\, a$, with a maximum value $D(r^*) \approx 2.1$ at melting (a = the characteristic interatomic distance of the system). This behavior appears

consistently across a wide variety of systems, including Lennard–Jones, Yukawa, Hard-Sphere, and Inverse-Power-Law models, suggesting the presence of a common underlying dynamical mechanism, as shown in Figure 1.

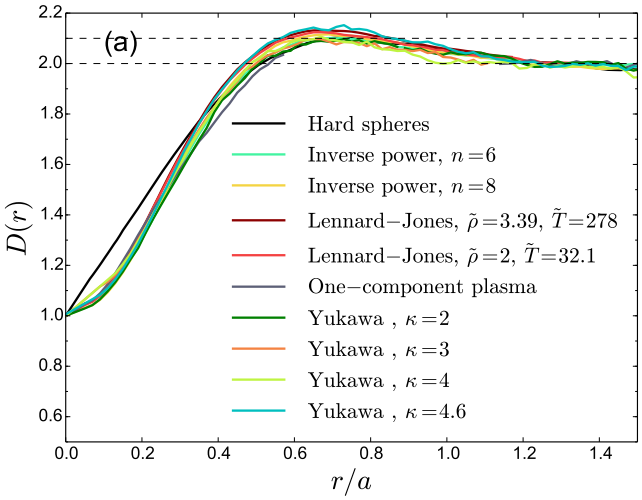

Figure 1: Mean first-passage statistics at freezing for diverse model liquids.

Building on this observation, we develop a melting criterion based solely on the liquid phase. Using only short *ab initio* trajectories, this criterion is able to reproduce the experimental melting curves of Al, Ti, and Li, without relying on phase-coexistence simulations or free-energy calculations.

From a physical standpoint, the peak in $D(r)$ signals the onset of a regime where atomic motion becomes temporarily localized. A minimal continuous-time random-walk model, defined by the vibrational spectrum and a single characteristic jump timescale, reproduces the emergence of this peak and indicates that the threshold corresponds to a critical degree of localization dominated by low-frequency vibrational modes. This establishes a direct connection between liquid dynamics and thermodynamic stability near the solid–liquid boundary, through a quantity that is both dimensionless and broadly transferable across interaction types.

This study focuses on monatomic model liquids and elemental metals, but extending the approach to multicomponent, molecular, or network-forming liquids represents a particularly promising direction for future research. Moreover, the current model-based interpretation does not yet provide an *a priori* derivation of the threshold $D(r^*) \approx 2.1$. Establishing a quantitative connection between this critical value, free-energy landscapes, and thermodynamic coexistence conditions remains an important objective for future work.

In this context, the main objective of this internship is to analyze and interpret the physical origin of the peak observed in the function $D(r)$ at the phase transition, using molecular dynamics simulations. The aim is to understand why the liquid systematically develops this distinctive dynamical signature near melting, and to relate it to the underlying atomic mechanisms that govern the onset of freezing.

During this internship, more than fifty Python and Fortran codes were developed or used. For this reason, the present report will focus primarily on the physical reasoning and scientific interpretation rather than on technical implementation. The full set of scripts will nevertheless be made available to the examination committee

during the oral presentation. The first part of the internship also involved becoming familiar with the Linux environment and learning to use LAMMPS; this preliminary work will not be detailed in this report.

2.2 Interparticle Potentials Studied

This project focuses on three representative interparticle potentials: **Lennard–Jones**, **Hard-Sphere**, and **Yukawa**. These models span a wide range of microscopic interactions and allow us to explore how the shape and range of a potential influence the structural and dynamical properties of liquids [31, 17].

2.2.1 Lennard-Jones potential

The **Lennard–Jones (LJ)** potential is a standard model for neutral atoms or nonpolar molecules. It combines short-range Pauli repulsion and long-range van der Waals attraction:

$$V_{\mathrm{LJ}}(r) = 4\varepsilon \left[\left(\frac{\sigma}{r}\right)^{12} - \left(\frac{\sigma}{r}\right)^{6} \right].$$

Here, ε sets the interaction strength and σ the distance where $V_{\mathrm{LJ}} = 0$. The LJ model successfully reproduces the basic phase behavior of simple liquids and serves as a reference for studying condensed-matter systems at the atomic scale [18, 19].

2.2.2 Yukawa potential

The **Yukawa** (or *screened Coulomb*) potential describes interactions that decay exponentially:

$$V_{\mathrm{Yukawa}}(r) = \varepsilon \, \frac{\exp(-\kappa r)}{r}.$$

The screening parameter κ controls the interaction range: small κ gives long-range forces, while large κ yields short-range interactions. This model is widely used for plasmas, dusty plasmas, ionic liquids, and charged colloids [20, 29, 22].

2.2.3 Hard-Sphere potential

The **Hard-Sphere (HS)** model represents particles interacting only through excluded volume:

$$V_{\mathrm{HS}}(r) = \begin{cases} \infty, & r < \sigma, \\ 0, & r \geq \sigma. \end{cases}$$

It contains no attraction; all properties arise purely from geometry. A key control parameter is the **packing fraction**:

$$\eta = \frac{\pi}{6} \, n^* \sigma^3,$$

which measures how much of the volume is occupied by the spheres. Increasing η drives the system from a dilute fluid to dense phases, glassy states, or crystallization [30, 24].

By comparing these three models—from purely repulsive hard spheres, to the balanced attraction–repulsion of Lennard–Jones, and the screened electrostatic forces of Yukawa—we investigate how microscopic interaction laws govern macroscopic observables such as structure, diffusion, and free-volume statistics in liquid systems.

2.3 Molecular Dynamics Software and Implementation

To study the interaction potentials introduced above, we performed molecular dynamics (MD) simulations using **LAMMPS** (Large-scale Atomic/Molecular Massively Parallel Simulator), an open-source package developed at Sandia National Laboratories [25]. LAMMPS integrates Newton's equations of motion to model the time evolution of interacting particle systems and is widely used for large-scale atomistic simulations in materials science, soft matter, and plasma physics.

LAMMPS includes many interatomic potentials (Lennard–Jones, Yukawa, EAM, Tersoff, etc.) and supports several thermodynamic ensembles (NVE, NVT, NPT) as well as various boundary conditions. Its modular and parallel architecture (MPI/OpenMP) makes it particularly efficient on high-performance computing clusters [26].

In this project, LAMMPS was used to generate atomic configurations and particle trajectories, which were then post-processed to extract structural and statistical properties such as the radial distribution function $g(r)$ and local free-volume distributions. These quantities, central to the characterization of liquids, follow classical theoretical frameworks described in statistical mechanics [31].

Because of its flexibility, LAMMPS requires a solid understanding of its input syntax and command structure. Once mastered, it allows the simulation of a broad range of atomic and molecular systems and the computation of numerous physical quantities, including particle positions, energies, pressure, temperature, and interaction forces.

2.4 Simulation Parameters

Running molecular dynamics simulations in LAMMPS requires choosing several key parameters that directly influence numerical stability, accuracy, and computational cost.

The **simulation box size** L sets the volume of the system and must be large enough to limit finite-size effects while preserving the target density. **Periodic boundary conditions** are applied to mimic an infinite bulk system and remove surface artifacts.

The **time step** dt determines the resolution of the integration of Newton's equations. It must be small enough to capture the fastest atomic motions (typically $1-2$ fs). The **total simulation time** must be long enough to ensure proper equilibration and to gather statistically meaningful averages.

The **cutoff radius** r_{cutoff} defines the maximum distance over which interactions are computed. Its value must balance accuracy and computational efficiency, especially for potentials with long tails such as Lennard–Jones or Yukawa.

Finally, the **number of particles** N controls the statistical representativeness of the system: larger systems reduce finite-size effects but increase computational cost.

Choosing appropriate values for L, N, dt, t_{tot}, and r_{cutoff} is therefore essential to obtaining reliable and reproducible molecular dynamics results.

2.5 Data Analysis and Post-Processing Tools

The analysis of data generated from molecular dynamics simulations requires efficient computational tools capable of handling large datasets and performing numerical treatments. In this work, we used programming languages such as **Python** and **Fortran**, as well as the visualization software **Gnuplot**, for post-processing and graphical analysis of simulation results.

Python was employed for data manipulation, statistical analysis, and visualization through libraries such as `NumPy`, `Matplotlib`, and `SciPy`. **Fortran** was used for high-performance numerical computations, particularly for the calculation of free volumes and histograms.

Gnuplot is an open-source plotting software that allows fast and precise visualization of data and analytical functions. It supports various output formats (PNG, PDF, EPS) and is especially convenient for automating the generation of scientific figures and fitting procedures.

Following the molecular dynamics simulations, several physical functions are computed using a `Fortran` code developed by Jérôme Daligault and Alfred Farris. This program mainly evaluates the functions $D(r)$, $\tau(r)$, $g(r)$, and MSD(t). It can be applied to all three interaction potentials considered in this study and serves as a foundation for the analysis of various physical quantities. For the functions $D(r)$ and $g(r)$, the results are expressed as a function of the reduced distance r/a, where a denotes the Wigner–Seitz radius.

The Wigner–Seitz radius a is defined as

$$a = \left(\frac{3}{4\pi n^*}\right)^{1/3}, \qquad n^* = \frac{N}{L^3} = \frac{\rho}{m}$$

where n^* is the particle number density. Physically, a represents the radius of a sphere that, on average, contains a single particle in a homogeneous system. It therefore provides a characteristic measure of the mean interparticle spacing. This length scale is widely used in plasma physics and condensed matter theory to normalize distances and to compare systems with different densities on a common, dimensionless basis. Table 1 summarizes the simulation parameters relevant to the calculation of the parameter a for each interaction potential.

Table 1: Simulation parameters for the Lennard–Jones, Yukawa, and Hard-Sphere models.

Parameter	**Symbol**	**Lennard–Jones**	**Yukawa**	**Hard Sphere**
Number of particles	N	variable	4000	512
Box length	L	$10.0\,\sigma$	$1.998 \times 10^{-6}\,\mathrm{cm}$	variable
Particle mass	m	1.0	$1.994 \times 10^{-23}\,\mathrm{g}$	N/A
Real density	ρ	variable	$0.01\,\mathrm{g\,cm^{-3}}$	variable
Boundary conditions	–	p p p	p p p	p p p
Integration units	–	reduced (LJ)	CGS	reduced (HS)
Wigner–Seitz radius	a	variable	$7.80871 \times 10^{-8}\,\mathrm{cm}$	variable

3 Analysis of the Logarithmic Derivative Curves

The first part of this internship consisted in reproducing the $D(r)$ curves of the Lennard–Jones, Yukawa, and Hard-Sphere models with the highest possible accuracy, in order to extract the transition parameters specific to each system with great precision. These calculations require selecting both an appropriate total simulation time and a suitable time step. The $D(r)$ curves for all three models are provided in Appendix 1. From these curves, we can extract the parameter values at the liquid–solid transition, as well as the values corresponding to $D(r) = 2.0$, where the peak first begins to develop. These quantities are essential for the remainder of this project and are reported in Table 2.

Value of $D(r)$	Lennard–Jones	Yukawa	Hard Sphere
2.1	$T_{\text{mel}} = 1.415$	$\Gamma_{\text{mel}} = 440.00$	$\eta_{\text{mel}} = 0.4953$
2.0	$T = 1.725$	$\Gamma = 390.00$	$\eta = 0.4779$

Table 2: Values of the transition parameters for the three interaction models.

4 Self-diffusion coefficient

The second part of this internship focuses on studying the self-diffusion coefficient of the investigated systems, with the goal of identifying a correlation between a slope break in its behavior and the emergence of the peak previously observed in the function $D(r)$.

The self-diffusion coefficient quantifies the ability of particles to move due to their own thermal motion, in the absence of external gradients. It reflects microscopic particle mobility and can be evaluated from molecular dynamics simulations using either the mean squared displacement (MSD) or the velocity autocorrelation function (VACF), following the Green–Kubo or Einstein relations [31, 32, 28].

The diffusion coefficient D is strongly temperature dependent: increasing T enhances particle kinetic energy and collision frequency, leading to higher diffusivity, while decreasing T causes motion to become progressively hindered by the potential-energy landscape and excluded-volume effects. This behavior is characteristic of thermally activated transport and is often described by an Arrhenius-type relation:

$$D = D_0 \exp\left(-\frac{E_a}{k_B T}\right),$$

where D_0 is a high-temperature pre-factor and E_a the activation energy.

In reduced units commonly used for Lennard–Jones, Yukawa, and Hard-Sphere systems, the inverse temperature can be expressed through dimensionless parameters such as the coupling parameter Γ or the packing fraction η. For Yukawa or Coulomb systems, the coupling parameter

$$\Gamma = \frac{Q^2}{4\pi\varepsilon_0 a k_B T}$$

measures the ratio of potential to thermal energy and therefore increases when the temperature decreases [29].

For Hard-Sphere systems, the relevant control parameter is the **packing fraction** η:

$$\eta = \frac{\pi}{6} n^* \sigma^3,$$

which quantifies the degree of crowding. Larger η reduces available free volume and decreases diffusion [30].

Thus, the parameters $1/T$, Γ, and η are closely related, as they all characterize the balance between thermal agitation and interparticle constraints. Variations in these quantities lead to similar trends in the diffusion coefficient, enabling a unified description of transport across different interaction potentials.

4.1 Mean Squared Displacement

The *Mean Squared Displacement* (MSD) is a physical quantity that measures the average squared distance traveled by particles as a function of time. It quantifies how far, on average, particles

move from their initial positions during a simulation or an experiment [31, 32]. The MSD is a key parameter used to characterize the diffusive behavior of a system and is defined as:

$$\mathrm{MSD}(t) = \left\langle |\mathbf{r}_i(t) - \mathbf{r}_i(0)|^2 \right\rangle \tag{1}$$

where $\mathbf{r}_i(t)$ is the position vector of particle i at time t, and the angle brackets $\langle \cdot \rangle$ denote an ensemble average over all particles. A linear increase of the MSD with time indicates normal diffusion, whereas deviations from linearity correspond to subdiffusive or constrained dynamics.

At long times, the MSD typically increases linearly with time, reflecting the diffusive regime of the system. In this regime, the self-diffusion coefficient D can be determined from the slope of the MSD according to the Einstein relation [33]:

$$D = \lim_{t \to \infty} \frac{\mathrm{MSD}(t)}{6t}. \tag{2}$$

4.2 Velocity Autocorrelation Function

The *Velocity Autocorrelation Function* (VACF) describes how the velocity of a particle at a given time is correlated with its velocity at a later time. It provides insight into the persistence of particle motion and the dynamical properties of the system [31]. The VACF is mathematically defined as:

$$C_v(t) = \langle \mathbf{v}_i(t) \cdot \mathbf{v}_i(0) \rangle \tag{3}$$

The integral of the VACF over time is directly related to the self-diffusion coefficient through the Green–Kubo relation:

$$D = \frac{1}{3} \int_0^\infty C_v(t)\, dt \tag{4}$$

Two complementary Python scripts were developed to analyze the microscopic diffusion behavior of the simulated systems. The first script calculates the velocity autocorrelation function, VAF(t), from the mean squared displacement (MSD) data using a finite-difference approximation of its second derivative. It processes all `msd.dat` files, computes the discrete second derivative of the MSD over time, and produces new files, `vaf.dat`, containing the corresponding VAF(t). This step converts the displacement information into a time-dependent measure of how particle velocities remain correlated, providing a direct view of how momentum relaxation occurs in the system.

The second script takes the computed VAF(t) and integrates it numerically using the trapezoidal rule to obtain the time-dependent diffusion coefficient, D(t), following the Green–Kubo relation. As time increases, D(t) gradually approaches a constant value, which corresponds to the self-diffusion coefficient D. The resulting `D.dat` files contain these integrated values and can be used to study the transition from the ballistic to the diffusive regime. Together, these two programs form a consistent post-processing workflow that links atomic motion from molecular dynamics trajectories to the macroscopic transport property of diffusion.

4.3 Results and Analysis

In a first step, we compared the evolution of the self-diffusion coefficient as a function of T_{mel}/T for the Lennard–Jones model for both methods (MSD and VAF). The self-diffusion coefficient was then calculated using the method based on the Velocity Autocorrelation Function, since this approach

is less influenced by the statistical noise introduced by molecular dynamics simulations. Next, we modified the parameter `r_seed` in LAMMPS, which defines the random seed used to initialize particle velocities at the start of each simulation for both the Lennard–Jones and Yukawa models. Changing this parameter allowed one to obtain several independent estimates of the self-diffusion coefficient for the same temperature (or the same value of Γ). The results were then averaged to minimize the effect of statistical noise and improve the reliability of the calculated diffusion values. The detailed parameters used for the Lennard–Jones and Yukawa simulations are summarized in Table 3.

Table 3: Simulation parameters for the Lennard–Jones and Yukawa models.

Parameter	**Symbol**	**Lennard–Jones**	**Yukawa**
Number of particles	N	1000	4000
Box length	L	$10.0\,\sigma$	$1.998 \times 10^{-6}\,\mathrm{cm}$
Particle mass	m	1.0	$1.994 \times 10^{-23}\,\mathrm{g}$
Time step	Δt	$0.001\,\tau_{\mathrm{LJ}}$	$1.0 \times 10^{-15}\,\mathrm{s}$
Total simulation time	t_{sim}	$2.5 \times 10^{4}\,\tau_{\mathrm{LJ}}$	$1.0 \times 10^{-10}\,\mathrm{s}$ (100 ps)
Temperature	T	variable	7703 K
Cutoff radius	r_{cut}	$6.0\,\sigma$	$4.685 \times 10^{-7}\,\mathrm{cm}$
Screening parameter	κ	–	$2.561 \times 10^{7}\,\mathrm{cm}^{-1}$
Potential strength	Γ	variable	variable
Boundary conditions	–	p p p	p p p
Integration units	–	reduced (LJ)	CGS

It is important to carefully convert the diffusion coefficients into the appropriate units. Indeed, the diffusion values are obtained from the MSD(t) data generated by the `Fortran` code in a common internal unit referred to as "mfpt". Consequently, the following equations are used to convert these results back into the reduced units corresponding to the Lennard–Jones and Yukawa systems:

$$\log(D_{\mathrm{LJ}}) = \log(D_{\mathrm{mfpt}}) - \tfrac{1}{2}\log(T^{*}) + \log\left(\tfrac{a}{\sigma}\right), \tag{5a}$$

$$\log(D_{\mathrm{Yukawa}}) = \log(D_{\mathrm{mfpt}}) - \tfrac{1}{2}\log(3\Gamma). \tag{5b}$$

For the Hard-Sphere model, we relied on a recent molecular dynamics studies on hard spheres [34], which provides diffusion coefficient values as a function of density. This allows us to determine the corresponding diffusion coefficients as a function of the packing fraction.
Then, the quantity $\ln(D)$ is plotted as a function of the reduced temperature T_{mel}/T, or equivalently, in terms of the reduced coupling parameter $\Gamma/\Gamma_{\mathrm{mel}}$ for the Yukawa model and the reduced packing fraction η/η_{mel} for the Hard-Sphere model. Then, we observe that certain regions of the plot exhibit a linear behavior. These portions are therefore fitted with straight lines of the form $y = ax + b$ in order to identify possible similarities between the three models (Figures 2 (a), 2 (b), 2 (c)).

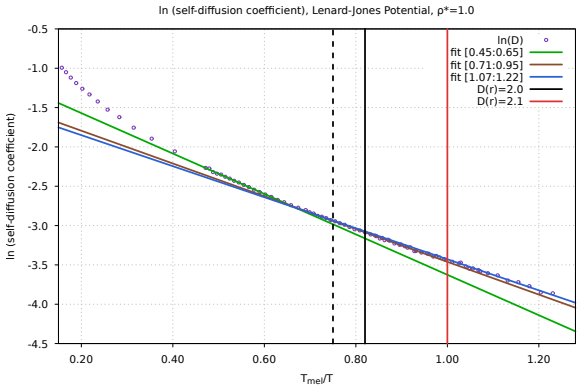

(a) Lennard–Jones model

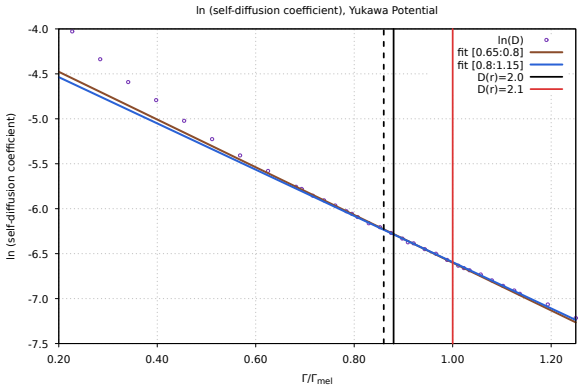

(b) Yukawa model

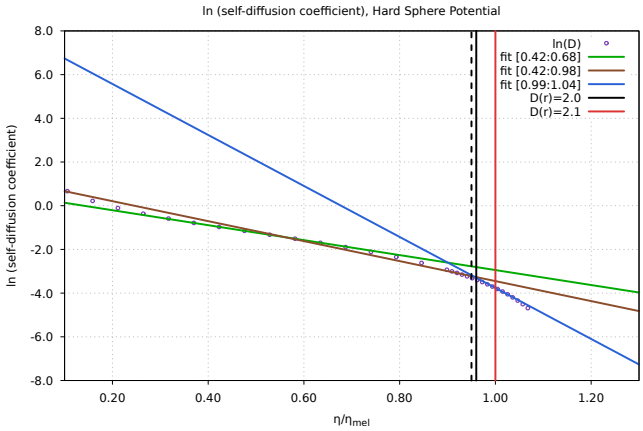

(c) Hard-Sphere model

Figure 2: Logarithm of the self-diffusion coefficient $\ln(D_{VAF})$ as a function of T_{mel}/T for Lennard–Jones (a), $\Gamma/\Gamma_{\text{mel}}$ for Yukawa (b), and η/η_{mel} for Hard-Sphere (c).

Examination of the three figures reveals that several fitted lines tend to intersect (black dashed lines) within the same region where the peak in the $D(r)$ curves corresponds to a value of 2.0 (black solid lines). This value of 2.0 corresponds, for all three models, to the onset of a peak in the $D(r)$ plots. It is therefore essential to understand, at the microscopic level, the physical mechanisms responsible for the emergence of this peak and to identify the phenomenon that gives rise to it.

5 Microscopic Study of the Free Volume

We recall here that the purpose of this study is to identify the microscopic mechanisms responsible for the development of a peak in the $D(r)$ curves, and consequently for the slope breaks observed in the behavior of the self-diffusion coefficient. In this section, we focus on a specific and conceptually straightforward physical quantity, the free volume available to a particle, which provides a microscopic framework for interpreting the observed diffusion behavior. Before moving on, it is important to introduce a physical function that will serve as the basis for our free-volume calculations: the radial distribution function $g(r)$, often called the pair correlation function.

5.1 The radial distribution function $g(r)$

The radial distribution function, $g(r)$, gives an idea of how the particles in a system are arranged around one another. It shows how the local density changes as a function of the distance r from a chosen reference particle. In practice, $4\pi r^2 g(r), dr$ represents the average number of particles found between r and $r + dr$. For an ideal gas, where the particles are randomly distributed, $g(r)$ equals 1 everywhere, meaning there is no preferred distance between particles. In contrast, in liquids or solids, $g(r)$ displays oscillations: the first peak corresponds to the most probable distance between two neighboring particles, while the following peaks reflect the degree of order in the surrounding structure. By looking at the shape of $g(r)$, one can therefore obtain direct information about the microscopic organization of the system and the nature of the interactions between particles.

This function makes it possible to identify the distances at which a particle's first, second, and higher coordination shells are found. In other words, it provides direct information about how neighboring particles are distributed in space around a reference particle.

5.1.1 Focus on the Hard-Sphere Model

In the Hard-Sphere model, particles are represented as perfectly rigid spheres that cannot overlap. There are no attractive forces between them, and the only interaction arises from the impenetrable core defined by the particle diameter σ. This simple constraint has a direct impact on the shape of the radial distribution function $g(r)$. For distances smaller than σ, $g(r)$ is strictly zero, since no particle can exist within the excluded volume of another. At $r = \sigma$, the function exhibits a sharp rise corresponding to the contact between neighboring spheres, which defines the most probable interparticle distance. Beyond this point, $g(r)$ oscillates around unity, showing alternating regions of higher and lower probability that reflect the spatial arrangement of successive coordination shells. As the system becomes denser, these oscillations become more pronounced, revealing the emergence of local order. Close to crystallization, the peaks of $g(r)$ align almost periodically, indicating a structure that approaches that of an ordered solid. Thus, the overall shape of $g(r)$ directly mirrors the geometric constraints and degree of packing characteristic of the Hard-Sphere system. The initial goal of this section is to generate the radial distribution function $g(r)$ for several packing fractions and to observe its main feature the hard, impenetrable wall that appears at contact between particles. A Fortran code developed several years ago by Jérôme Daligault is used to generate all the data for the Hard-Sphere model, including particle positions, energies, and the radial distribution function $g(r)$, among others. However, the code does not directly allow us to set or predict the packing fraction η. Instead, the simulations are controlled through a variable parameter r, which effectively determines the degree of compression of the system. By varying this parameter, we can indirectly modify the packing fraction and thus explore different densities of the Hard-Sphere system. After adjusting the Fortran code, I was able to generate a correspondence table between the parameter r and the packing fraction η, as detailed in Appendix (Table A.1), and to generate Figure 3, which shows the radial distribution function $g(r)$ as a function of the diameter σ.

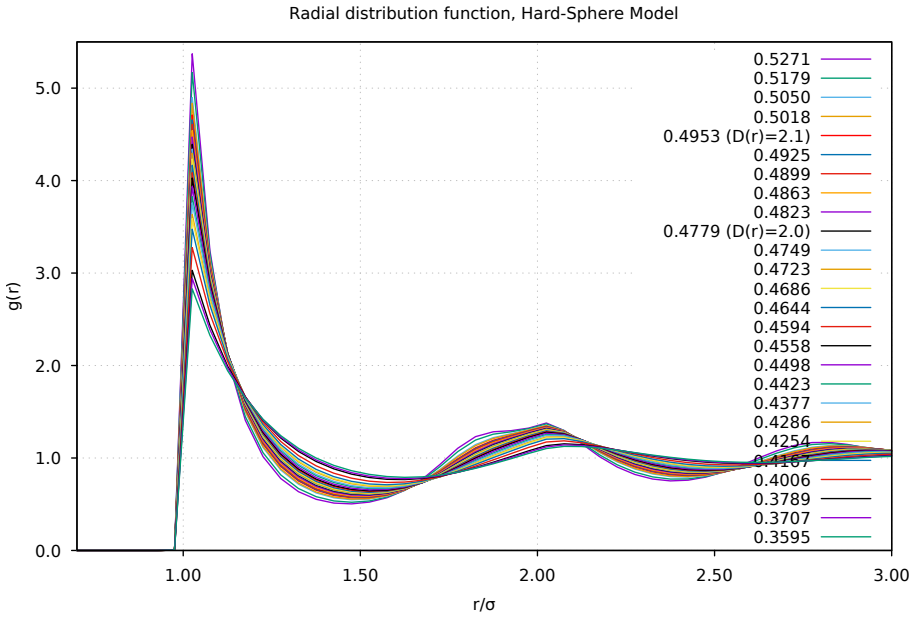

Figure 3: Radial distribution function, Hard-Sphere model.

This figure confirms that particles cannot overlap, and that the minimum center-to-center distance between them is $r/\sigma = 1.0$. Furthermore, the first minimum observed around $r/\sigma \approx 1.44$ corresponds to the distance to the first coordination shell, i.e., the position of the nearest neighboring particles. We will use this notion of the first coordination shell in the calculations of the free volumes.

5.2 A first calculation of the free volume

In order to understand the physical mechanism behind the peak observed in $D(r)$ and the slope break in the self-diffusion coefficient, we first introduce the concept of free volume. To do so, we refer back to the minimal model inspired by the seminal ideas of Frenkel [32] and Zwanzig [33], who described atomic motion in liquids as a combination of localized vibrations and occasional spatial jumps an approach particularly relevant near the freezing transition. Two main quantities must therefore be considered in this framework: localized vibrations and spatial jumps. When a particle diffuses, that is, when it moves from one position to another, it must have enough free space available to do so meaning that its nearest neighbors do not completely fill the surrounding volume. This is precisely where the notion of free volume comes into play. We will compute the free volume available around a particle at a given time t, and then average this quantity over all particles. The goal is to detect whether a change in free volume occurs at the freezing transition.

To begin with, we focus exclusively on the Hard Sphere model, since it is by far the simplest framework to work with. In this description, particles behave like solid billiard balls whose volumes cannot overlap, which automatically sets a strict minimum separation between them. This avoids the complications that arise in the Lennard-Jones or Yukawa models, where the notion of a minimum distance is not fixed because the interactions are soft and allow particles to approach more gradually.

5.2.1 Free-Volume Calculation Method

As mentioned earlier, particles in the Hard Sphere model cannot approach each other closer than r=1.0 σ, so each sphere has an effective radius of 0.5 σ. For our analysis, we gather the position files from all the Hard Sphere simulations carried out at different packing fractions.

The first step is to extract particle positions only at specific, regularly spaced times so that the configurations are sampled evenly. After that, we need to wrap the particles back into the L-length simulation box. "Wrapping" means that whenever a particle crosses one side of the periodic box, we bring it back from the opposite side, ensuring that all positions remain inside the boundaries of the box. The free volume calculation is performed by analyzing the local environment of each particle in a given Hard Sphere configuration. For every particle, the script places a radius R spherical probe around its center and determines how much of this sphere is occupied by neighboring particles. To do so, the positions of all particles are combined with their periodic images, and a KD–tree search is used to efficiently identify neighbors whose own spherical volumes intersect the probe. A KD-tree (short for k-dimensional tree) is a data structure that allows very fast searches of neighboring points in space. Instead of checking the distance between one particle and all the others which would be extremely slow for large systems — the KD-tree organizes the points in a hierarchical, tree-like structure. This makes it possible to quickly eliminate large regions of space that are too far away to matter. As a result, finding all the neighbors within a radius R becomes much faster, typically scaling as $\mathcal{O}(\log N)$ rather than $\mathcal{O}(N)$. This is why KD-trees are widely used in molecular simulations, computer graphics, and any application where one needs to repeatedly search for nearby points in a large set.The occupied volume is obtained either from the full volume of a neighboring sphere (when it lies entirely inside the probe) or from the analytical expression of the intersection between two spheres when only partial overlap occurs. The free volume associated with the particle is then defined as the difference between the probe volume and the total occupied volume. This procedure is repeated for all particles and for multiple simulation snapshots, and the resulting free volumes are averaged and normalized by the particle volume, providing a quantitative measure of the available local space as a function of the probe radius R. In the free–volume calculation, the central particle is deliberately excluded from the evaluation of the occupied volume. As a consequence, for small probe radii, the free volume starts at 0%, since the probe sphere is fully filled by the particle located at its center. If the central particle were included in the computation, the free volume would instead start artificially at 100%, because the probe volume would simply coincide with the particle's own volume. By removing the central particle from the count, the free volume grows only once the probe radius exceeds the particle's hard core, providing a physically meaningful measure of the space available around it. The free volumes obtained from this procedure are presented in Figure 3. A free-volume calculation was also performed on an FCC structure to validate the method used in this work. We also computed the first and second derivatives of the free-volume curve obtained while excluding the central particle from the calculation (Figure 3). The goal of this additional analysis is to highlight very subtle variations in the free-volume behavior that are not immediately visible from the raw curve alone. As a preliminary step, we also verified that our Hard-Sphere simulations are physically realistic by computing the average number of neighbors up to σ=1.5. To do so, we used the following relation:

$$N(1.0, 1.5) = 4\pi\rho \int_{1.0\sigma}^{1.5\sigma} r^2\, g(r)\, dr, \quad \text{with} \quad g(\sigma^+) = \frac{1-\eta/2}{(1-\eta)^3} \quad \text{(value of } g \text{ at contact)}.$$

According to the literature [44], the average number of neighbors within 1.5σ (the first coordination number) around a particle in a Hard-Sphere system, for large packing fractions, is approximately

12. This analysis allowed us to confirm the reliability of our Hard-Sphere simulation (see Appendix A.1).

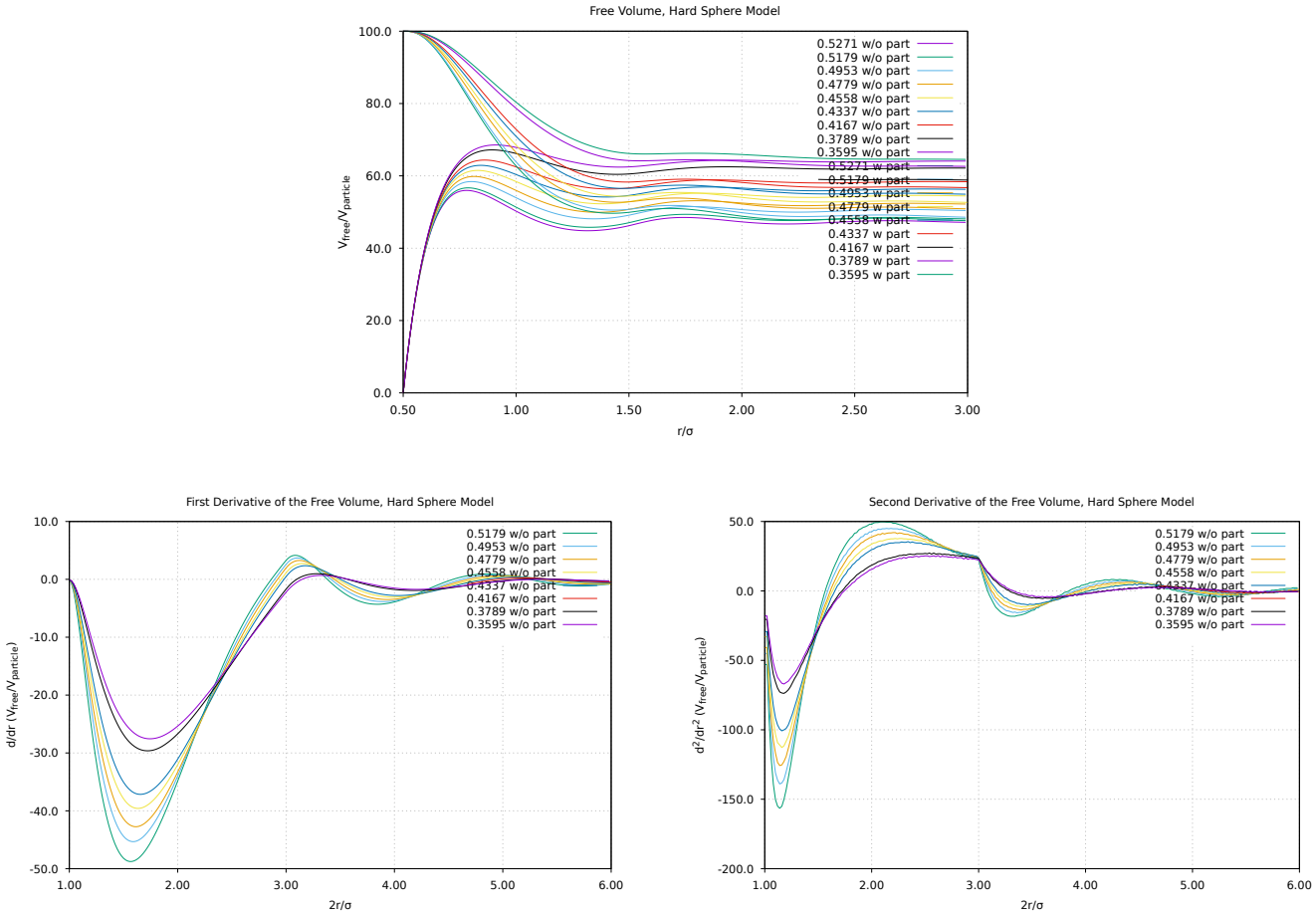

Figure 4: Free-volume curve (top) and its first and second derivatives (bottom).

Looking at the free-volume curve, we observe that its asymptotic behavior is fully consistent with the expected packing fractions. In particular, when the probe radius R becomes very large, the free volume normalized by the particle volume naturally approaches the packing fraction of the system. This is exactly what we should obtain, since at very large R the probe sphere samples the entire simulation domain and therefore reflects the global fraction of space occupied by the particles. Unfortunately, no meaningful physical interpretation can be drawn from these figures at this stage, particularly around 1.5σ. This means that we will need to revisit the notion of free volume with more care and develop a more refined and intuitive way of interpreting it.

5.3 A second calculation of the free volume

To correctly evaluate the free volume available to each particle, it is essential to consider an exclusion radius equal to σ around every neighbor, rather than the physical particle radius $\sigma/2$. This follows from the fact that the free volume is defined with respect to the position of the particle's center and not its geometric boundary. In a hard-sphere system, two particles come into contact when their centers are separated by exactly σ; consequently, the region into which the center of a particle cannot penetrate is a sphere of radius σ around each neighbor. Using

$\sigma/2$ would only describe the space occupied by the particle itself, but would not reflect the true steric constraints imposed by surrounding particles, leading to a strong overestimation of the free volume. By adopting σ as the exclusion radius, the calculation captures the correct center-to-center constraints that govern local packing, cage formation, and dynamical hindrance in dense fluids. This choice ensures that the computed free volume reflects the physically accessible space for the particle's center within the many-body environment.[35] [43]

5.3.1 Free-Volume Calculation Method and Fortran Implementation

The `free_volume` program computes the free volume accessible around each particle of a three-dimensional system by combining neighbor detection, periodic boundary conditions, and a spherical discretizations of space. After reading an input control file, the program extracts the total number of particles, the number of particles used for the analysis, the particle diameter σ, the maximum cavity radius $R_{\max}$, and the names of the input/output files. The atomic coordinates are then read from a LAMMPS-style file that specifies the simulation box bounds and the particle positions. The box lengths L_x, L_y, and L_z are reconstructed, and all subsequent distance calculations use the minimum-image convention to ensure that periodic boundary conditions are correctly imposed.

The first computational step is a full neighbor search. For each particle, the program loops over all other particles, computes the relative displacement corrected by periodicity, and identifies those whose distance is smaller than a cutoff radius $R_{\max,\mathrm{nn}}$. These neighbors are stored along with their image-corrected positions. During this process, the code also determines the minimum interparticle distance for each particle, which identifies its closest neighbor. This information is important because it sets the maximum radius a spherical cavity can reach before intersecting another particle.

Once the local environment of each particle is known, the code proceeds to the free-volume calculation. The space around each particle is discretized radially, with the radius $r = dr$, $2dr$, ..., $R_{\max}$, and angularly using a fine spherical grid consisting of n_θ polar angles and n_ϕ azimuthal angles. For a given radius r, two situations are possible. If r is smaller than the clearance up to the closest neighbor ($r \leq R_m = d_{\min} - \sigma$), the entire spherical region of that radius is free of overlap, and the free volume is simply the full geometric volume $V_f = \frac{4\pi r^3}{3}$. If $r > R_m$, overlap with neighbors may occur, and the free volume must be evaluated numerically. In this case, the program scans all angular directions: for each pair (θ, ϕ), it constructs a test point at distance r from the particle center, checks whether this point lies inside the excluded hard-core region of any neighbor (i.e. at distance $< \sigma$), and accumulates the corresponding differential volume element $r^2 \sin\theta \, dr \, d\theta \, d\phi$ whenever the point is admissible. Summing all accessible angular directions yields the free volume at radius r for that particle.

This procedure is repeated for all radii and all particles. The program stores the free-volume function $V_f(i, r)$ for each particle and writes several outputs: (i) the average free volume $\langle V_f(r) \rangle$ as a function of radius, which characterizes the typical amount of free space in the system; and (ii) a file listing, for each particle, the free volume at selected radii of physical interest (such as $r = \sigma_{\mathrm{eff}}$, 1.50 (at hollow) and 1.96 (at the second peak). Overall, the code provides a detailed numerical estimation of the local free volume in a dense hard-sphere or Lennard-Jones fluid, accurately capturing how the presence of neighboring particles restricts the available space around each atom. To improve the clarity of the free-volume interpretation, this quantity is illustrated in Figure A.8, which is included in the Appendix. The free volumes will be expressed in units of the volume of a sphere, i.e., $V_{\mathrm{free}} / \left(\frac{\pi \sigma_{\mathrm{eff}}^3}{6} \right)$.

We must carry out the same analysis for the Yukawa and Lennard-Jones models. The main difficulty is that these two interaction potentials do not feature a well-defined physical diameter σ_{eff}, since particles may overlap depending on the softness of the potential. Therefore, an effective hard-sphere diameter must be introduced in order to map these systems onto an equivalent hard-sphere model. This effective diameter σ_{eff} then serves as a consistent length scale for comparing the free-volume behavior across the different interaction models.

5.3.2 Computation of the effective diameters σ_{eff} for the Yukawa and Lennard–Jones models

- Lennard-Jones : In this work, we rely on two standard definitions of the effective diameter for the Lennard–Jones potential: the Ben-Amotz–Herschbach (BAH) diameter [37] and the LWCA–AH diameter, obtained from the Lado-modified Weeks–Chandler–Andersen theory [38]. These two approaches are widely used in the liquid-state literature to map a Lennard–Jones fluid onto an equivalent hard-sphere system [39]. The BAH diameter is defined through an integration of the repulsive part of the potential and depends only on the reduced temperature T*:

$$\sigma^*_{\text{BAH}}(T^*) = 1.1532 \left[1 + (1.8975\, T^*)^{1/2}\right]^{-1/6}.$$

The LWCA–AH approach provides a more accurate estimate of the effective diameter, especially at high densities, since it incorporates both temperature and density effects. The analytical expression used here is

$$\sigma^*_{\text{LWCA-AH}}(T^*, \rho^*) = 1.1152 \left[1 + \sqrt{T^* T^*_0(\rho^*)}\right]^{-1/6},$$

where T^* and ρ^* are reduced variables, and $T^*_0(\rho^*)$ is a density-dependent function.

Both effective diameters will be used throughout the following sections in order to compare, on a consistent length scale, the free-volume behavior obtained from the Lennard–Jones, Yukawa, and Hard-Sphere models.

- Yukawa : Unlike the Lennard–Jones potential, the Yukawa interaction does not possess a well-defined or commonly adopted effective diameter. Because the potential is soft and allows for partial overlap between particles, different definitions of σ_{eff} exist in principle, but none of them has emerged as a standard in the literature. In order to compare the Yukawa system with the Hard-Sphere reference, we follow a more pragmatic approach: we determine an effective diameter by aligning the Yukawa data with the Hard-Sphere behavior. In practice, this consists in choosing σ_{eff} such that a selected structural or dynamical quantity (for example the contact value of the radial distribution function, or the position of the first peak) of the Yukawa fluid collapses onto the corresponding Hard-Sphere curve. This mapping provides a consistent length scale that allows us to analyse the free-volume properties of the Yukawa model within the same framework as the Lennard–Jones and Hard-Sphere systems.

5.3.3 Results and Analysis

The free-volume curves obtained for the Lennard–Jones and Yukawa models are shown in Figure A.4 in the Appendix. As illustrated in Figure 5(a) for the Hard-Sphere model, the free volume

reaches a plateau rather quickly at high packing fractions (corresponding to large values of Γ for the Yukawa potential and low temperatures for the Lennard–Jones system). This behavior indicates that, beyond a certain radius, no additional accessible space becomes available to the particle's center: the local environment is already fully constrained by neighboring particles. In other words, the particle becomes effectively caged, and the shape of the free-volume curve reflects the strong steric hindrance that characterizes dense fluids in the vicinity of the freezing transition.

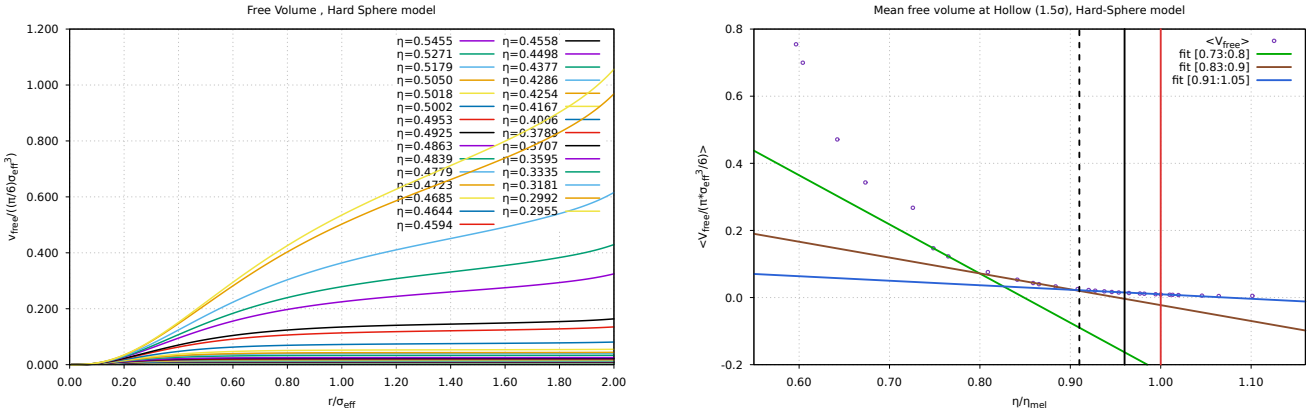

(a) Free volume distribution

(b) Mean free volume at the hollow

Figure 5: Free volume analysis for the Hard-Sphere model: (a) free volume distribution, (b) mean free volume at the hollow.

We now focus on the free volume at the hollow (i.e., the first minimum) of the radial distribution function $g(r)$ for the three interaction potentials. This minimum corresponds to the first coordination shell surrounding each particle. This shell is of particular interest, as it determines whether a particle has sufficient space to diffuse.

As can be observed in Fig. 5(b) for the Hard-Sphere model, and in Appendix (Fig. A.5 (a) and (b) for the Yukawa and Lennard–Jones models, the free volume at the hollow appears to decrease exponentially with the packing fraction (or with Γ for the Yukawa model and with $1/T^*$ for the Lennard–Jones model). A plateau also seems to emerge for the three models around the packing fraction at which the peak in $D(r)$ begins to develop. This further supports the idea that the behavior of $D(r)$ is directly linked to the microscopic dynamics occurring within the first coordination shell.

To deepen the analysis, we now turn our attention to the distribution of the natural logarithm of the free volume at the hollow for each model. Examining $\ln(v_{\text{free}})$ is particularly insightful, as free-volume fluctuations are typically highly skewed and span several orders of magnitude. Taking the logarithm therefore compresses the dynamic range, highlights the statistical structure of rare events, and often reveals whether the underlying distribution follows a log-normal or stretched-exponential behavior [42, 43]. This representation thus provides a more robust way to compare the microscopic free-volume statistics across different interaction potentials.

The resulting histograms (Appendix, Figs. A.6 (a) and (b) for the Yukawa and Lennard–Jones models) exhibit a shape that is remarkably close to a skew-normal distribution. A skew-normal distribution is a generalized form of the Gaussian distribution characterized by three parameters: a location parameter ξ, a scale parameter w, and a shape parameter α that controls the degree and direction of asymmetry [40, 41]. When $\alpha = 0$, the distribution reduces to a symmetric Gaussian;

non-zero values of α produce left- or right-skewed profiles. In dense liquids, such skewness naturally reflects the asymmetric fluctuations of the cage formed by neighboring particles.

The probability density function of the skew-normal distribution is

$$f(x;\xi,w,\alpha) = \frac{2}{w}\,\phi\left(\frac{x-\xi}{w}\right)\Phi\left(\alpha\,\frac{x-\xi}{w}\right),$$

where ϕ and Φ denote the standard normal PDF and CDF, respectively. In our case, the fitted variable is $x = \ln(v_{\text{free}})$, so the corresponding distribution of the free volume is obtained through a change of variables:

$$p_v(v) = \frac{1}{v}\,f(\ln v;\xi,w,\alpha).$$

This formulation provides a compact and physically meaningful way to characterize the asymmetric microscopic fluctuations of the free volume. We were thus able to successfully fit all the histograms using a skew-normal distribution, as shown for the Hard-Sphere model at the transition packing fraction (Fig. 6).

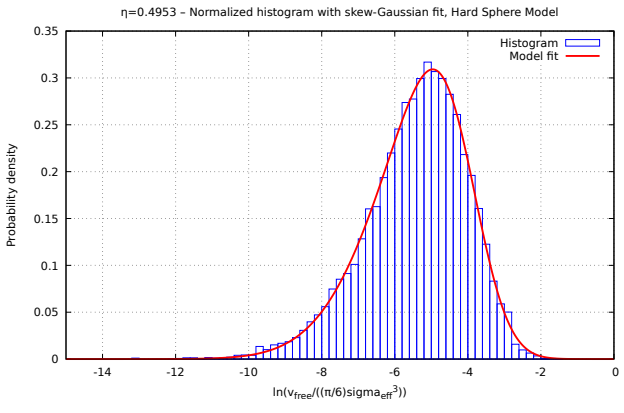

Figure 6: Histogram of $\ln(v_{\text{free}})$ for the Hard-Sphere model.

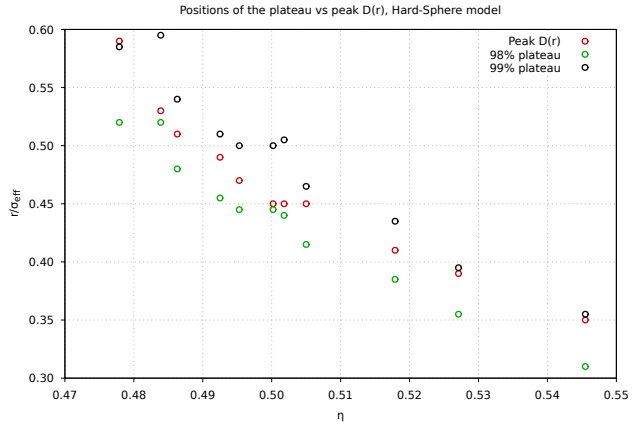

Figure 7: Plateau positions vs peak $D(r)$ for the Hard-Sphere model.

These mathematical analyses will later allow us to confirm, in a future scientific publication, that the skew-normal shape observed in the free-volume histograms is not a numerical artifact but a robust and characteristic feature of the physical systems studied. The asymmetry in the distribution of $\ln(v_{\text{free}}/[(\pi/6)\sigma^3_{\text{eff}}])$ reflects the microscopic fluctuations of free volume in dense liquids. Demonstrating the universality of this skew-normal profile across different interaction potentials will further strengthen its physical relevance and support the interpretation of dynamical signatures near the freezing transition.

Finally, we examine in more detail the free-volume curves as a function of distance. We observe that the positions of the peaks in $D(r)$ systematically coincide with the distances at which the free volume reaches its plateau. As shown in Fig. 7 for the Hard-Sphere model, and in Appendix Figs. A.7 for the Yukawa and Lennard–Jones systems, the peak in $D(r)$ always appears when the free volume has reached between 98% and 99% of its plateau value for Lennard–Jones and Hard–Sphere, and between 99.85% and 99.97% for the Yukawa potential.

This consistent correspondence suggests a direct physical connection between the onset of dynamical hindrance (captured by the peak in $D(r)$) and the saturation of the available free volume

around each particle.

A direct connection emerges between the peak of $D(r)$ and the point at which the free-volume curve reaches its plateau. At small r, particles remain trapped within their local cages, and the available free volume increases rapidly with distance, resulting in a low and slowly varying $D(r)$. As r increases, the system reaches a critical distance at which the free volume becomes almost saturated typically between 98% and 99.9% of its asymptotic value, depending on the interaction model. At this point, even a small increase in available space produces a sharp change in particle mobility, which manifests as a pronounced maximum in $D(r)$. Beyond this region, once the free volume has fully plateaued, additional space no longer significantly alters the dynamics, and $D(r)$ decreases accordingly. This correspondence indicates that the dynamical transition captured by $D(r)$ the escape from the local cage occurs precisely when the structural environment provides enough free volume for diffusion to take place.

6 Conclusion

After 24 weeks of internship at Los Alamos National Laboratory, this project has led to substantial scientific progress. We have established a clear link between the emergence of a peak in the $D(r)$ function and the microscopic mechanisms governing particle diffusion, consistently observed across three interaction models: Lennard–Jones, Yukawa, and Hard Sphere. These advances were made possible through extensive molecular-dynamics simulations and the development of dedicated analysis tools, including numerous Python and Fortran codes designed to process, visualize, and interpret the resulting data.

Given the complexity and breadth of the work carried out, summarizing these results in twenty pages has been particularly challenging. Many technical choices, computational strategies, and methodological decisions could only be briefly outlined here. The oral presentation to be held in January will therefore provide a valuable opportunity to discuss these elements in greater depth.

Beyond the scientific results, this internship has been an exceptionally formative experience. Entering a research environment with limited prior exposure to programming, molecular dynamics, and advanced theoretical concepts required sustained effort, but proved profoundly rewarding. I am grateful for the trust placed in me by my supervisor and for the guidance that made this work possible.

Finally, following my mentor's proposal, this collaboration will continue remotely from France through secure access to the laboratory's computational resources. This extension will allow us to further investigate the mechanisms underlying the peak observed in $D(r)$ and to assess whether this criterion can be applied to other systems, such as water models. In the longer term, this continued effort is expected to lead to a scientific publication based on the results obtained during this internship.

7 Bibliography

References

[1] L. Hoddeson, P. W. Henriksen, R. A. Meade, and C. Westfall, *Critical Assembly: A Technical History of Los Alamos during the Oppenheimer Years, 1943–1945*, Cambridge University Press, 1993.

[2] R. Serber, *The Los Alamos Primer: The First Lectures on How to Build an Atomic Bomb*, University of California Press, 1992.

[3] K. Bird and M. J. Sherwin, *American Prometheus: The Triumph and Tragedy of J. Robert Oppenheimer*, Vintage, 2006.

[4] R. Rhodes, *The Making of the Atomic Bomb*, Simon and Schuster, 1986.

[5] F. G. Gosling, *The Manhattan Project: Making the Atomic Bomb*, U.S. Department of Energy, 2014.

[6] Los Alamos National Laboratory, *LANL History Overview*, (Accessed 2024). Available at: `https://www.lanl.gov`.

[7] S. S. Hecker, "LANL and its Evolving Mission," *Physics Today*, 2017.

[8] Los Alamos National Laboratory, *Annual Report 2023*. Available at: `https://www.lanl.gov`.

[9] Los Alamos National Laboratory / NNSA, *Trinity Supercomputer Overview*, 2022.

[10] Los Alamos National Laboratory, *LANL Strategic Plan 2023*. Available at: `https://www.lanl.gov`.

[11] G. de With, "Melting is well-known, but is it also well-understood?" *Chemical Reviews*, **123**, 13713–13795 (2023). "

[12] M. Frost *et al.*, "High-pressure melt curve and phase diagram of lithium," *Physical Review Letters*, **123**, 065701 (2019).

[13] D. N. Polsin *et al.*, "Structural complexity in ramp-compressed sodium to 480 GPa," *Nature Communications*, **13**, 2534 (2022).

[14] J. P. Hansen and D. Schiff, "Influence of interatomic repulsion on the structure of liquids at melting," *Molecular Physics*, **25**, 1281–1290 (1973).

[15] A. M. J. Schaeffer, W. B. Talmadge, S. R. Temple, and S. Deemyad, "High-pressure melting of lithium," *Physical Review Letters*, **109**, 185702 (2012).

[16] E. Gregoryanz, O. Degtyareva, M. Somayazulu, R. J. Hemley, and H.-K. Mao, "Melting of dense sodium," *Physical Review Letters*, **94**, 185502 (2005).

[17] D. Chandler, *Introduction to Modern Statistical Mechanics*, Oxford Univ. Press (1987).

[18] J.E. Jones, "On the determination of molecular fields," *Proc. Roy. Soc. A* **106**, 441 (1924).

[19] L. Verlet, "Computer experiments on classical fluids. I," *Phys. Rev.* **159**, 98 (1967).

[20] H. Yukawa, "On the interaction of elementary particles," *Proc. Phys.-Math. Soc. Japan* **17**, 48 (1935).

[21] S. Hamaguchi, R. Farouki, and D. Dubin, "Triple point of Yukawa systems," *Phys. Rev. E* **56**, 4671 (1997).

[22] V. Fortov et al., "Complex (dusty) plasmas," *Phys. Usp.* **47**, 447 (2004).

[23] B.J. Alder and T.E. Wainwright, "Phase transition in elastic disks," *J. Chem. Phys.* **27**, 1208 (1957).

[24] P.N. Pusey and W. van Megen, "Observation of a glass transition in suspensions of hard spheres," *Phys. Rev. Lett.* **59**, 2083 (1987).

[25] S. Plimpton, "Fast Parallel Algorithms for Short-Range Molecular Dynamics," *J. Comput. Phys.* **117**, 1–19 (1995).

[26] A.P. Thompson *et al.*, "LAMMPS – a flexible simulation tool for particle-based materials modeling at the atomic, meso, and continuum scales," *Comput. Phys. Commun.* **271**, 108171 (2022).

[27] M. P. Allen and D. J. Tildesley, *Computer Simulation of Liquids*, Oxford University Press (2017).

[28] D. Frenkel and B. Smit, *Understanding Molecular Simulation*, Academic Press (2002).

[29] S. Hamaguchi, R. T. Farouki, and D. H. E. Dubin, "Triple point of Yukawa systems," *Phys. Rev. E* **56**, 4671 (1997).

[30] B. J. Alder and T. E. Wainwright, "Phase Transition for a Hard Sphere System," *J. Chem. Phys.* **27**, 1208 (1957).

[31] J.-P. Hansen and I. R. McDonald, *Theory of Simple Liquids*, Academic Press (2013).

[32] M. P. Allen and D. J. Tildesley, *Computer Simulation of Liquids*, Oxford University Press (2017).

[33] A. Einstein, "On the motion of small particles suspended in liquids at rest," *Annalen der Physik* **17**, 549 (1905).

[34] Pieprzyk, S., Bannerman, M. N., Branka, A. C., Chudak, M. & Heyes, D. *Thermodynamic and dynamical properties of the hard sphere system revisited by molecular dynamics simulation.* Phys. Chem. Chem. Phys. **21**, 6886–6899 (2019).

[35] Hoover, W. G., Hoover, N. E. & Hanson, K. *Exact hard-disk free volumes.* J. Chem. Phys. **70**, 1837–1844 (1979).

[36] S. Sastry, T. M. Truskett, P. G. Debenedetti, S. Torquato, and F. H. Stillinger, *Free volume in the hard sphere liquid*, Molecular Physics, **95**(2), 289–297 (1998).

[37] Hamaguchi, S., Farouki, R. T. & Dubin, D. H. E. *Physical properties of Yukawa fluids*. Journal of Chemical Physics **105**, 7641–7650 (1996).

[38] Silva, C. M., Liu, H. & Macedo, E. A. *Comparison between Different Explicit Expressions of the Effective Hard Sphere Diameter of Lennard-Jones Fluid: Application to Self-Diffusion Coefficients*. Ind. Eng. Chem. Res. **37**, 221–227 (1998).

[39] Chandler, D., Weeks, J. D., & Andersen, H. C. *Van der Waals Picture of Liquids, Solids, and Phase Transformations*. Science **220**, 787–794 (1983).

[40] Azzalini, A. *A class of distributions which includes the normal one*. Scandinavian Journal of Statistics **12**, 171–178 (1985).

[41] Azzalini, A. & Capitanio, A. *Distributions generated by perturbation of symmetry with emphasis on a multivariate skew t-distribution*. Journal of the Royal Statistical Society B **65**, 367–389 (2003).

[42] Costa, M., Hecht, E., Donley, E. & Perkins, T. *Skewed statistical distributions in physical systems*. American Journal of Physics **69**, 691–697 (2001).

[43] Sastry, S., Truskett, T. M., Debenedetti, P. G., Torquato, S. & Stillinger, F. H. *Free volume in the hard sphere liquid*. Molecular Physics **95**, 289–297 (1998).

[44] Trokhymchuk, A., Nezbeda, I., Jirsák, J. & Henderson, D. *Hard-sphere radial distribution function again*. J. Chem. Phys. **123**, 024501 (2005).

Appendices

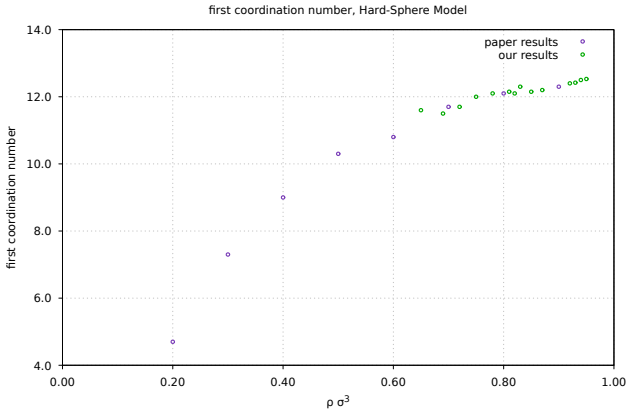

Figure A.1: First coordination number and comparison with literature results.

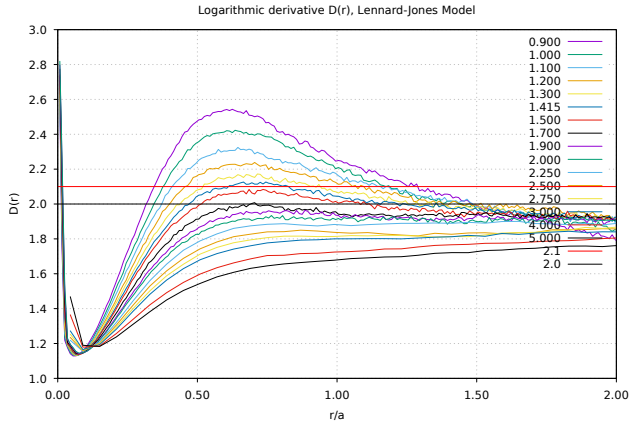

Figure A.2: $D(r)$ curve for the Lennard–Jones model.

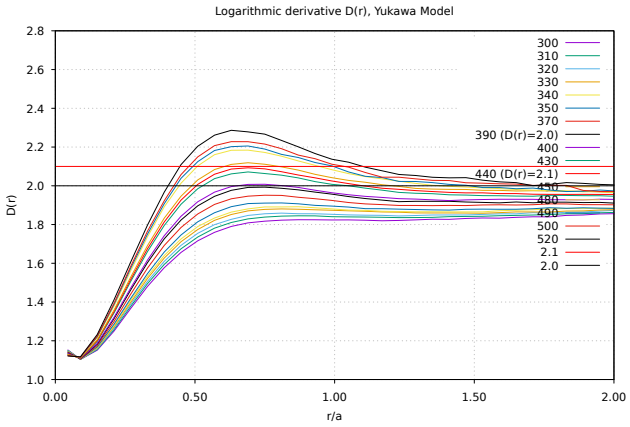

(a) $D(r)$ curve for the Yukawa model.

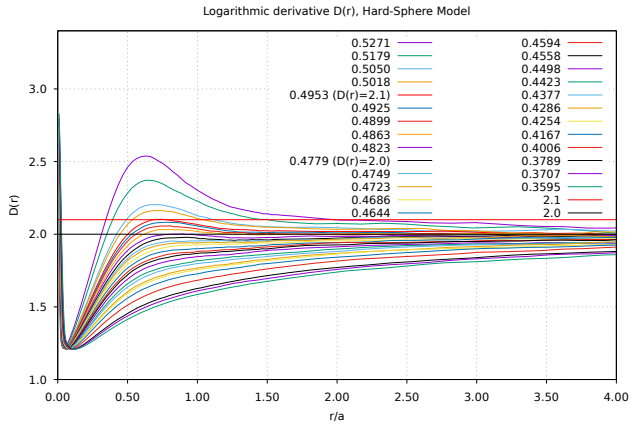

(b) $D(r)$ curve for the Hard-Sphere model.

Figure A.3: $D(r)$ curves for the Yukawa (left) and Hard-Sphere (right) models.

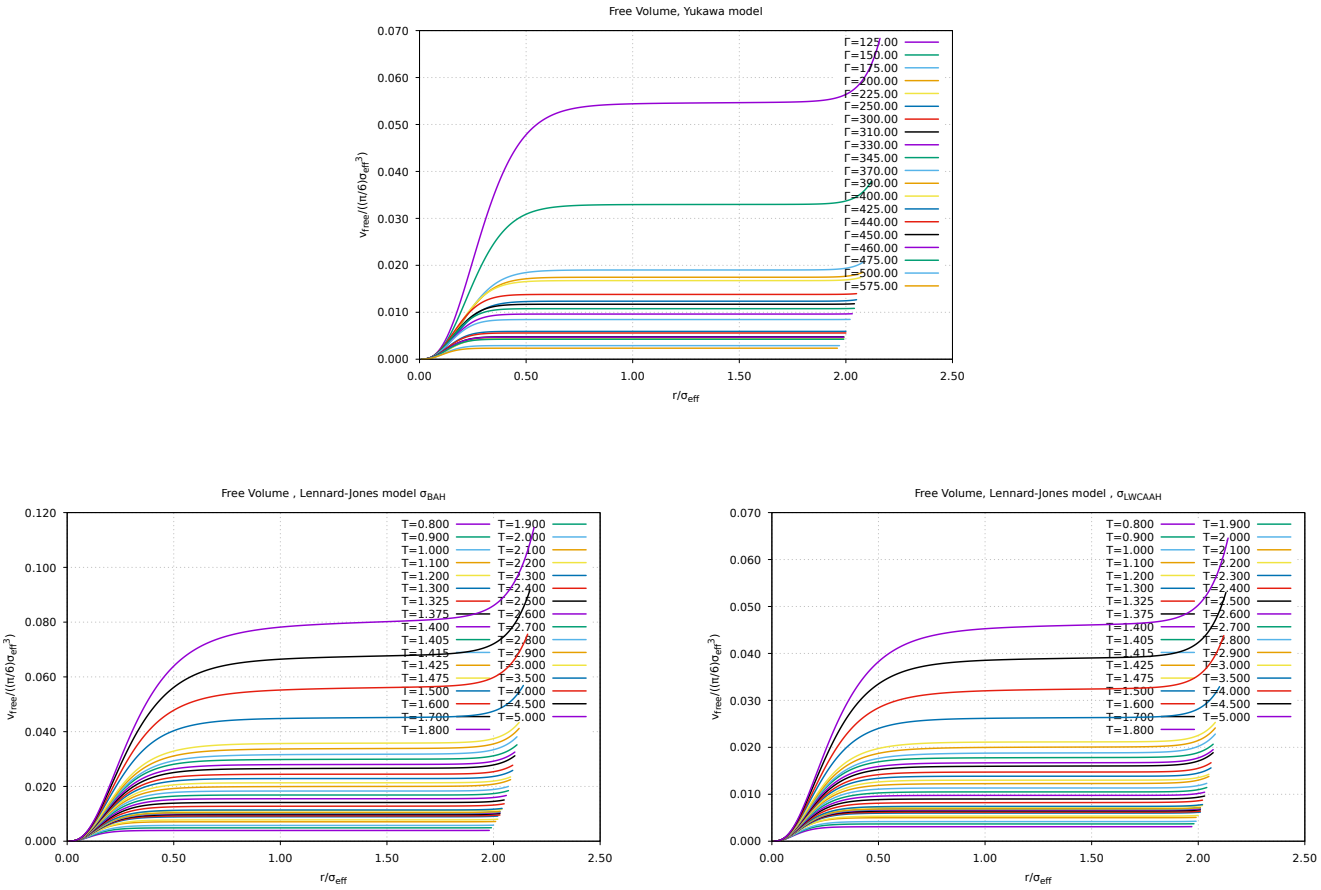

Figure A.4: Free Volume Figures for the Yukawa model (top), LJ-BAH (bottom left), and LJ-LWCAAH (bottom right).

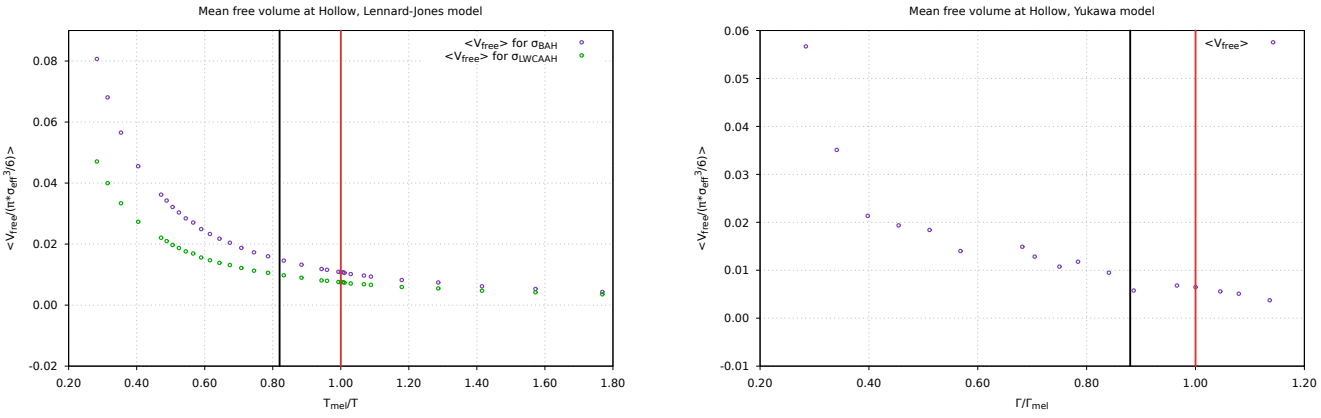

(a) Lennard–Jones (b) Yukawa

Figure A.5: Mean free volume at Hollow for the LJ (left) and Yukawa (right) models.

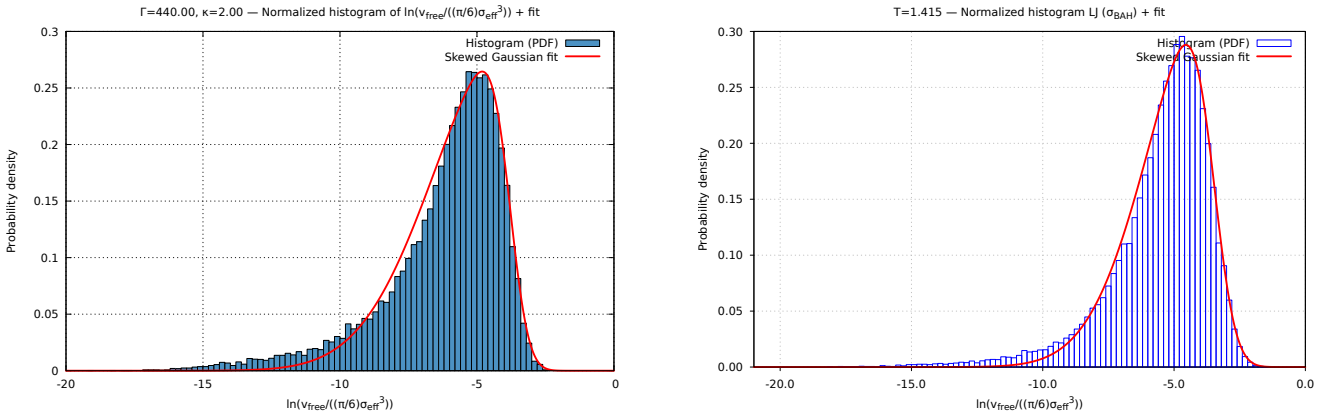

(a) Yukawa model

(b) LJ model

Figure A.6: Histograms of ln(vfree) for the Yukawa (left) and the LJ-BAH (right) models

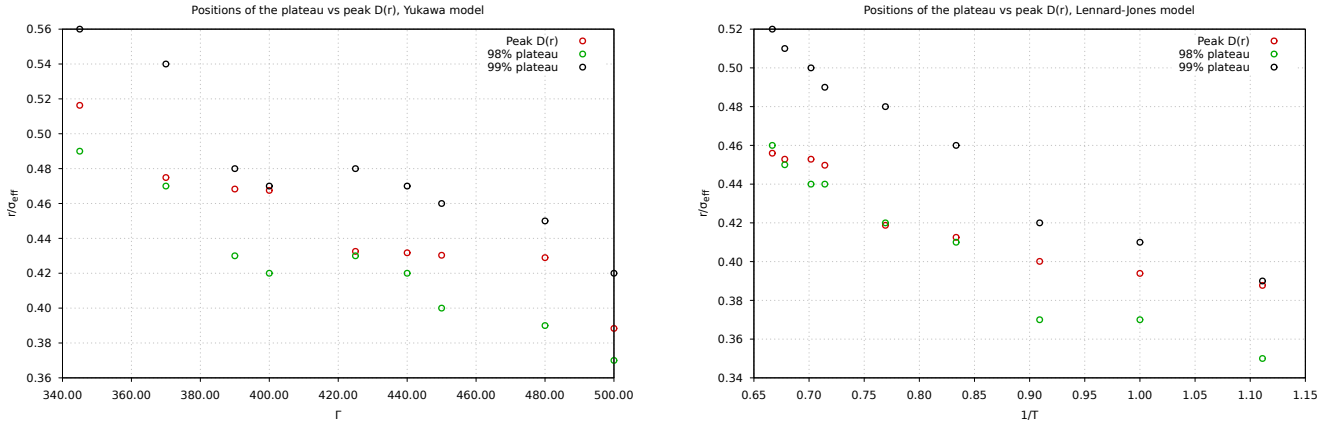

(a) Yukawa model

(b) Lennard–Jones model

Figure A.7: Comparison of the plateau positions and peak $D(r)$ for (a) the Yukawa model and (b) the Lennard–Jones model.

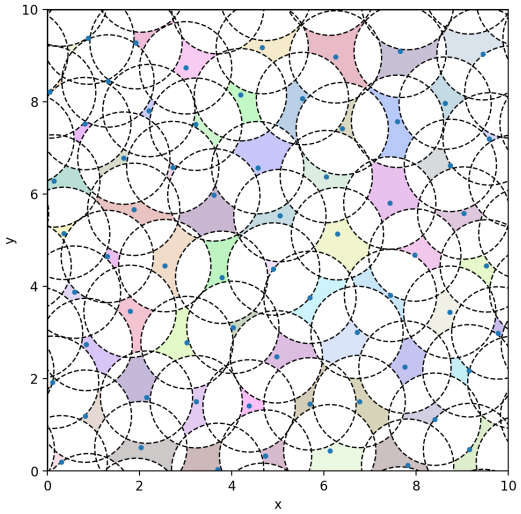

Figure A.8: Theoretical Visualization of the Free Volume in 2D, Hard Sphere model

Table A.1: Correspondence between the parameter r and the packing fraction η for the Hard-Sphere model.

Parameter r	**Packing fraction** η
0.0300	0.5455
0.0400	0.5271
0.0500	0.5179
0.0600	0.5050
0.0650	0.5018
0.0675	0.5002
0.0700	0.4953
0.0750	0.4925
0.0800	0.4853
0.0825	0.4839
0.0900	0.4779
0.1000	0.4685
0.1100	0.4644
0.1150	0.4594
0.1200	0.4558
0.1300	0.4498
0.1500	0.4377
0.1700	0.4286
0.1800	0.4254
0.2000	0.4167
0.2400	0.4006
0.3200	0.3789
0.3600	0.3707
0.4000	0.3595